

Maud Rise revisited

R. D. Muench,¹ J. H. Morison,² L. Padman,¹ D. Martinson,³ P. Schlosser,³
B. Huber,³ and Roland Hohmann³

Abstract. An oceanographic field program called the Antarctic Zone Flux experiment was carried out in the eastern Weddell Sea during austral winter (July–September) 1994. Data from a drift buoy array were used in concert with shipboard observations to provide exceptionally high horizontal resolution of upper ocean hydrographic parameters near Maud Rise. Chemical and tracer data were obtained from the ship. We identify a “warm pool” southwest of the rise as a dynamically necessary region of positive (cyclonic) vorticity that is associated with a Taylor column over the rise. Both a warm “halo” surrounding the Taylor column and the warm pool are associated with thermocline shoaling that is a necessary condition for high upward heat fluxes to occur. These features extend the influence of Maud Rise bottom topography on upper ocean heat flux over a region that is larger, by a factor of at least 2, than the area directly overlying the rise. Areal mean upward heat fluxes of about 25 W m^{-2} are derived using both upper ocean T (“instantaneous”) values and tracer data (“integrated”) values. Fluxes derived over the warm halo and pool regions using only upper ocean T exceeded 100 W m^{-2} at specific sites. Elsewhere in the region, the T -derived heat fluxes varied widely from <10 to $>50 \text{ W m}^{-2}$, whereas the tracer-derived heat fluxes showed a considerably more uniform distribution. Our mean values are similar to those that have been previously reported. Historical ice cover data have shown that the geographical region encompassed by Maud Rise and the warm pool area to the southwest is a preferred site for polynya formation, consistent with these findings. Time series analyses of the historical upper ocean data set suggest that conditions conducive to polynya formation are correlated with climate processes remote from the Southern Ocean.

1. Introduction

Much of the initial mixing between ambient Weddell Sea Warm Deep Water (WDW) and Circumpolar Deep Water (CDW) that flows southwestward into the Weddell Sea from the Antarctic Circumpolar Current (ACC) occurs in the Weddell Sea near Maud Rise. The easternmost limb of the Weddell Gyre between about longitudes 10°W and 40°E , where the ACC is deflected southward in response to regional bathymetric trends, is where CDW first encounters the colder and less saline WDW that typifies the northern limb of the Weddell gyre. The ensuing combination of WDW and CDW, rich in mesoscale features and not yet well mixed, comprises the source water that moves west-southwestward into the Maud Rise region.

Vertical density gradients in the eastern Weddell Sea are small compared with those in most of the world ocean. Vertically averaged N^2 for the uppermost 500 m, below which there is very little vertical density gradient, is of order 10^{-6} s^{-2} . The currents are consequently strongly barotropic and influenced by bottom topography as shown, for example, in the observations by *Gouretski and Danilov* [1993] of the ACC path east of Maud Rise. Even the ice concentration appears to be influ-

enced by topography, as *De Veaux et al.* [1993] estimated that $>50\%$ of the variability in Antarctic sea ice concentration could be explained by topographic influences.

The combined WDW and CDW encounters Maud Rise, a seamount of order 100 km in diameter that extends upward from the 5000 m deep abyssal plain to within 1600 m of the sea surface. The impingement of these waters upon Maud Rise initiates a number of dynamic events. An isolated column of water becomes at least partially trapped over the rise and has been characterized as a Taylor column [*Ou*, 1991; *Alverson and Owens*, 1996]. Water in this column, which blocks horizontal flow over the rise, is colder, less saline, and slightly denser than the surrounding waters. Regional southwestward flow is accelerated around the periphery of the column, causing a ring-shaped closed circulation about the rise of the relatively warm and saline combined WDW and CDW. The closed circulation cell, which we will refer to as the Maud Rise halo or simply the “halo,” has a complex structure with sharp fronts and multiple warm cores [*Gordon and Huber*, 1990; *Bersch et al.*, 1992]. The surrounding regional flow continues southwestward past the rise and contributes more or less continuously to a downstream region of water with elevated T that is situated southwest of the rise and that we will refer to as the “warm pool.”

The water column overlying Maud Rise, the halo, and the warm pool downstream (west-southwest) from the rise each locally influence ocean processes. These features impact particularly strongly the local upper ocean heat fluxes and associated overlying air-sea exchanges [*McPhee et al.*, 1996], and their integrated effect can be expected to influence strongly regional upper ocean heat and ice budgets. Upward doming of the warm underlying core waters within individual mesoscale

¹Earth & Space Research, Seattle, Washington.

²Polar Science Center, Applied Physics Laboratory, Seattle, Washington.

³Lamont-Doherty Earth Observatory, Palisades, New York.

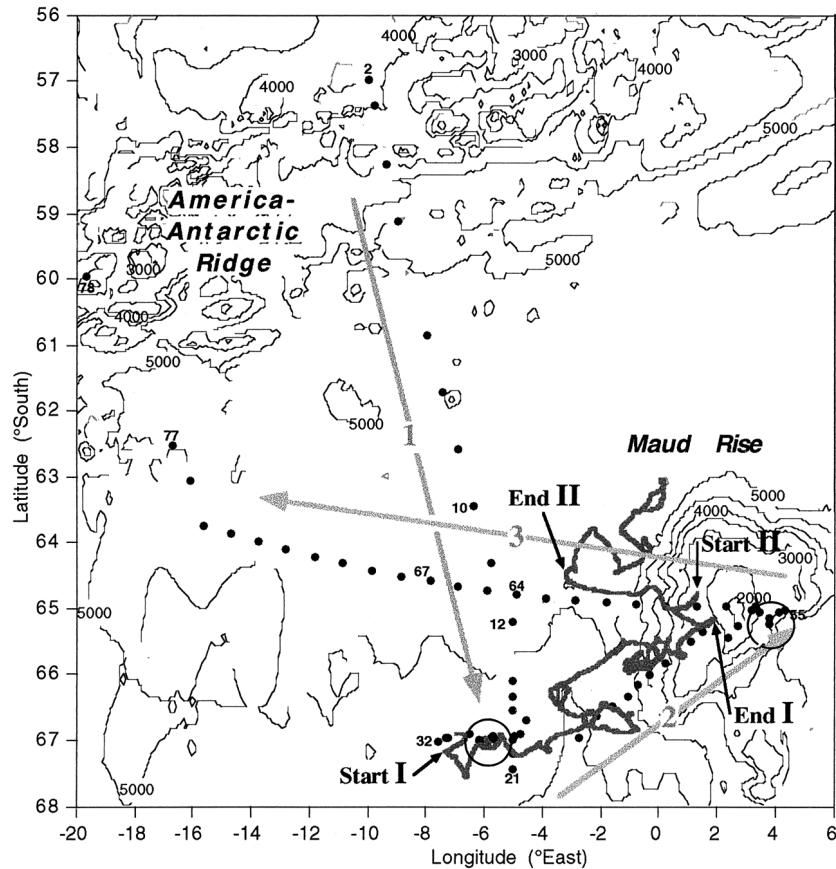


Figure 1. Location of the ANZFLUX field program. Solid circles indicate the locations of shipboard conductivity-temperature-depth (CTD) stations. Long shaded arrows labeled 1, 2, and 3 indicate the orientations and directions of occupation of shipboard transects 1, 2, and 3, while small numbers adjacent to selected CTD station sites indicate station numbers at the ends of these transects. The bold line shows the Polar Ocean Profile (POP) buoy drift trajectory. The start and end points of the drift trajectory segments used to construct buoy transects I and II are labeled “Start I,” “Start II,” “End I,” and “End II.” Bottom contours, shown at 1000 m intervals, were obtained from the ETOPO5 data set. Open circles indicate sites for the two drifting stations.

features, many of them probably eddies, enhances upward heat flux from the deep waters to the upper mixed layer [McPhee *et al.*, 1996] and increases the quantity of heat available for melting ice. Lateral advection, relative to deeper waters, of the upper layers overlying Maud Rise can lead to conditions favorable to vigorous vertical mixing, which then locally enhances upward heat flux from below the pycnocline to the surface mixed layer (L. Padman *et al.*, Cabeling and low-density ratio diffusive convection in the Weddell Sea, submitted to *Journal of Geophysical Research*, 2000, hereinafter referred to as Padman *et al.*, submitted manuscript, 2000).

Heat flux results obtained during Antarctic Zone Flux (ANZFLUX) have been discussed on the basis of physical observations [McPhee *et al.*, 1996, 1999; Padman *et al.*, submitted manuscript, 2000]. A detailed discussion of the distribution of dissolved oxygen (DO) and helium (He) isotopes during ANZFLUX in terms of entrainment of WDW into the winter mixed layer and the related oceanic heat flux is given by R. Hohmann *et al.* (^3He and dissolved oxygen in the upper waters of the Weddell Sea: Implications for oceanic heat fluxes, submitted to *Journal of Geophysical Research*, 2000, hereinafter referred to as Hohmann *et al.*, submitted manuscript, 2000). Despite this recent work, however, we still do not understand

the physical mechanisms that apparently couple the local bottom topography with the high upper ocean heat fluxes. Neither do we know the impact of these mechanisms on the upper ocean over the geographical region beyond the more obvious local effects of the topography. Finally, we do not have good large area estimates of the regional upper ocean heat fluxes or their spatial distribution, areal mean, and maximum values. With these questions in mind, this paper focuses on the ocean features that are associated with Maud Rise and assesses their impact upon the regional oceanography and the heat budget.

2. Data Collection and Processing

The ANZFLUX field program took place from the ice-strengthened research vessel ice breaker (RVIB) *Nathaniel B. Palmer* in the eastern Weddell Sea region overlying and west of Maud Rise during austral winter (July–August) 1994 (Figure 1). The program consisted of spatially nested experiments. Shipboard measurements were taken at discrete stations along three regional transects. Small-scale observations at two ship-based drifting stations, each about 6 days in length, measured vertical heat fluxes and associated small-scale processes in the upper ocean and across the air-ice-ocean interface. Two drift-

ing buoys were deployed directly following completion of the first drifting station; they measured distributions of temperature and salt along their irregular trajectories through the study region. Observations on the regional transects were limited to the upper ocean from the surface down to 1500 m, to 500 m in the case of the drift stations, and to 200 m for the drifting buoys. These depth limitations were consistent with the ANZFLUX experimental focus on upper ocean processes.

2.1. Regional Shipboard Transects

Stations were occupied from the ship along three regional transects (Figure 1). Transect 1 extended southward from near the America–Antarctic Ridge to the region southwest of Maud Rise (stations 2–21). Transect 2 extended northeastward from near the southern end of transect 1 onto the rise (stations 32–55). Transect 3 extended westward from the rise, finally veering northward and exiting the study region (stations 55–77). Station spacing was about 100 km on transect 1 except in its more intensively sampled extreme southern portion, about 25 km along most of transect 2, and about 50 km along transect 3.

Vertical profiles of T , conductivity (C , subsequently used to compute S) and DO were taken down to 1500 m at each ship station using a SeaBird SBE-911 conductivity-temperature-depth (CTD) system. Upper layer current profiles were measured using a hull-mounted 150 kHz RDI acoustic Doppler current profiler (ADCP) that was operated at each CTD site and continuously during the two drifting stations. The ensemble averaging period was 60 s, 8 m vertical bin sizes were used, and profiles were typically obtained to depths exceeding 300 m.

Each of the CTD casts on the regional transects was augmented by water samples obtained using a rosette sampler. Samples for DO analysis were collected from Niskin bottles and analyzed using a modified Winkler titration based on an automatic titrator with amperometric endpoint detection. The combined sampling and analytical error expressed as 1 standard deviation derived from replicate samples is 0.04 mL L⁻¹. Water samples for noble gas analysis were collected from Niskin bottles and stored in sealed copper tubes. He and Ne isotope measurements were conducted at the Noble Gas Laboratory (NGL) of the Lamont-Doherty Earth Observatory (for details, see *Ludin et al.* [1998]). Concentrations of ³He are reported as relative deviations of the measured helium isotope ratio ($R = [^3\text{He}]/[^4\text{He}]$) from that of air, $\delta^3\text{He}(R/R_{\text{atm}} - 1)100\%$, with $R_{\text{atm}} = 1.384 \times 10^{-6}$ [*Clarke et al.*, 1976]. The precision of $\delta^3\text{He}$ is about $\pm 0.2\%$. The helium isotope ratio of water in solubility equilibrium with the atmosphere is smaller than that in the atmosphere ($R_{\text{eq}}(-1.87^\circ\text{C}, 34 \text{ psu}) = 1.359 \times 10^{-6}$; $\delta^3\text{He}_{\text{eq}} = -1.8$, *Benson and Krause* [1980]) since ³He is slightly less soluble than ⁴He.

2.2. Drifting Buoy Sections

Two instrumented buoys were deployed about 200 m apart on the same ice floe on July 30, 1994, and left to drift with the ice, returning data and position information through the Argos satellite system. One of these, a Polar Ocean Profile (POP) buoy provided by the University of Washington, used SeaBird SeaCat CTDs to measure water T and C (yielding S) every 12 min at nominal depths of 10, 70, and 150 m. The POP buoy sensors are accurate in typical applications to about 0.01°C in T and 0.02 psu in S . This buoy drifted along an irregular trajectory northeastward toward Maud Rise, veering northward and then slightly westward into open water around No-

vember 28, and ceased transmitting on December 6, 1994 (Figure 1). A similar buoy provided by the Alfred Wegener Institute was also deployed and returned a shorter record over a similar trajectory (not shown). The buoys were ice-mounted rather than drogued. Consequently, their trajectories reflected wind-driven ice motion rather than underlying water movement.

The POP buoy data analysis utilized the cable motion caused by speed changes that were associated with the start and end of periods of rapid ice drift. As drift speed increased, the cable and sensors were deflected sideways and upward by frictional drag exerted by the relatively slow moving water column. With decreasing drift speed the cable returned to vertical, and the sensors deepened to their nominal depths. The three sensors consequently sampled over a range of depths shallower than their nominal depths. The data from 74 such vertical excursions, which we refer to as “castlets” to differentiate them from conventional CTD casts, were averaged over 10 m depth bins to produce 0–150 m distributions of T and S that were measured along the buoy trajectory. Segments of the trajectory roughly paralleled the ship transects and lagged the transects by weeks to months. This allowed comparison of upper ocean features at two different times along buoy drift sections I and II that roughly paralleled shipboard CTD transect 2 and the eastern portion of transect 3, respectively (Figure 1).

3. Oceanic Features in the Eastern Weddell

The shipboard, POP buoy, and drifting station data allow a more detailed description of the upper ocean features associated with Maud Rise than could be constructed using solely shipboard data. The ship data are presented in a vertical section as three deep transects (0–1500 m) showing distributions of T , S , and density (Figures 2–4) and as shallow transects (0–200 m) showing the distributions of DO concentration and $\delta^3\text{He}$ value (Plate 1). The shipboard and POP buoy data are combined in order to yield two intensively sampled upper layer (0–150 m) transects that focus on the area immediately west of Maud Rise (Plates 2–3). The combined shipboard and buoy data are then used to construct horizontal maps of T and S over the same restricted area (Plate 4).

3.1. Regional Features

Ship transect 1 illustrates the regional meridional distributions of T , S , and density (Figure 2). Temperatures exceeding 1.5°C at 400 m depth mark the core of the ACC at the north end of the transect. The ACC water was bounded on its south by a frontal structure extending down to at least 1500 m (the maximum depth sampled). South of this structure lay a zone of order 100 km in meridional extent (although the large station spacing precludes a reliable estimate of its breadth) having the lowest maximum T (<0.5°C) along the transect. This region of low T was consistent with the presence of an eastward extending remnant of the Weddell–Scotia Confluence (WSC) water that originates in the vicinity of the northern terminus of the Antarctic Peninsula and extends roughly along the America–Antarctic Ridge. Farther south, maximum T increased to a typical range of 0.5°–0.75°C, and parcels of water having $T > 0.9^\circ\text{C}$ and $S > 34.69 \text{ psu}$ were present at the south end of the transect.

The remaining two deep transects show regional structure in the zonal plane extending from Maud Rise to about 1000 km west from its crest (Figures 3–4). Maximum T was lower over

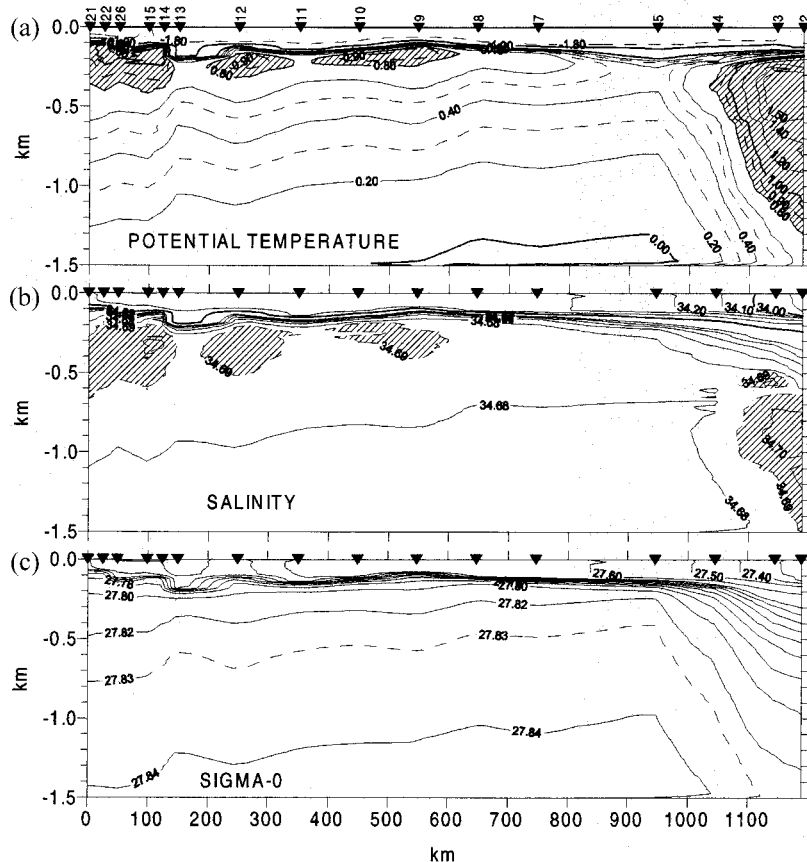


Figure 2. Distributions of (a) T , (b) S , and (c) σ_0 along north-south regional shipboard transect 1, constructed using data from shipboard CTD casts. Hatched regions correspond, for comparison purposes, to the hatched values shown on Figure 4 of *Gordon and Huber* [1990]. Solid triangles show station sites, and numbers along the top axis are corresponding station numbers.

the Rise (about 0.6°C) than farther west, as was S (by about 0.02 psu). The western flank of the rise was overlain by a pronounced warm saline feature ($T > 1.0^\circ\text{C}$ and $S > 34.7$ psu) that comprised the halo. Maximum warm core T gradually decreased toward the west, though this decrease was interrupted at irregular intervals by warmer parcels, until the west-northwest extreme end of the transect (stations 74–77) where the warm-core T reached its lowest values (except for those overlying Maud Rise and in the WSC water) of $0.5^\circ\text{--}0.75^\circ\text{C}$. Mixed layer depths were about 110 m except overlying the halo and where associated with anomalous warm-core features.

The regional T and S distributions that were observed during winter 1994 qualitatively resembled those documented in earlier work [e.g., *Gordon and Huber*, 1990; *Bersch et al.*, 1992]. The warm regime was not well defined, and the cold regime as defined by $T < 0.5^\circ\text{C}$ was not encountered as core temperatures were always above 0.5°C except in the WSC just south of the ACC, as noted above. Our failure to encounter the cold regime may reflect interannual variability in its extent and may also reflect warming in the WDW layer as reported for the past several years by *Fahrbach et al.* [1998]. *Gordon and Huber* [1990] documented the upper 1000 m particularly well near Maud Rise and observed maximum temperatures in 1986 of $1.0^\circ\text{--}1.2^\circ\text{C}$ overlying the flanks of Maud Rise. We observed similar temperatures over the flanks of the rise in 1994. The vertical extent of the warm halo was also about the same in

1994 as in 1986. The width of the feature in a direction radial from the center of Maud Rise was, however, only about 100 km in 1994 compared with 200 km documented by *Gordon and Huber* [1990]. Their observations show what appear to be two concentric warm cores associated with the halo, consistent with our observations. The upper layer density that we observed in winter 1994 was almost identical to values from previous years, reaching about $\sigma_0 = 27.79$ over the center of the rise. The total density difference from the surface to 500 m in the eastern portion was about 0.04 sigma units ($N^2 \approx 10^{-6} \text{ s}^{-2}$).

Ocean-ice-atmosphere interactions in the vicinity of Maud Rise have been parameterized, in terms of upper ocean T , S , and density distributions, by *Martinson and Iannuzzi* [1998] and are similar to those in the core of the Weddell Gyre farther west. In terms of mean winter heat flux the Maud Rise region occupies the extreme southwestern portion of a spatially coherent region that extends northward to the boundary of the gyre and represents extremes in the climatological variables presented by *Martinson and Iannuzzi* [1998].

The regional DO and $\delta^3\text{He}$ distributions in the upper 200 m, illustrated along ship transect 2, were typical of upper waters in the central Weddell Sea during austral winter (Plate 1). WDW was characterized by high $\delta^3\text{He}$ values (average = $8.64 \pm 0.22\%$) and low DO (average = $4.49 \pm 0.06 \text{ mL L}^{-1}$) concentrations (*Hohmann et al.*, submitted manuscript, 2000). Entrapment of ^3He -rich and DO-poor WDW into the winter

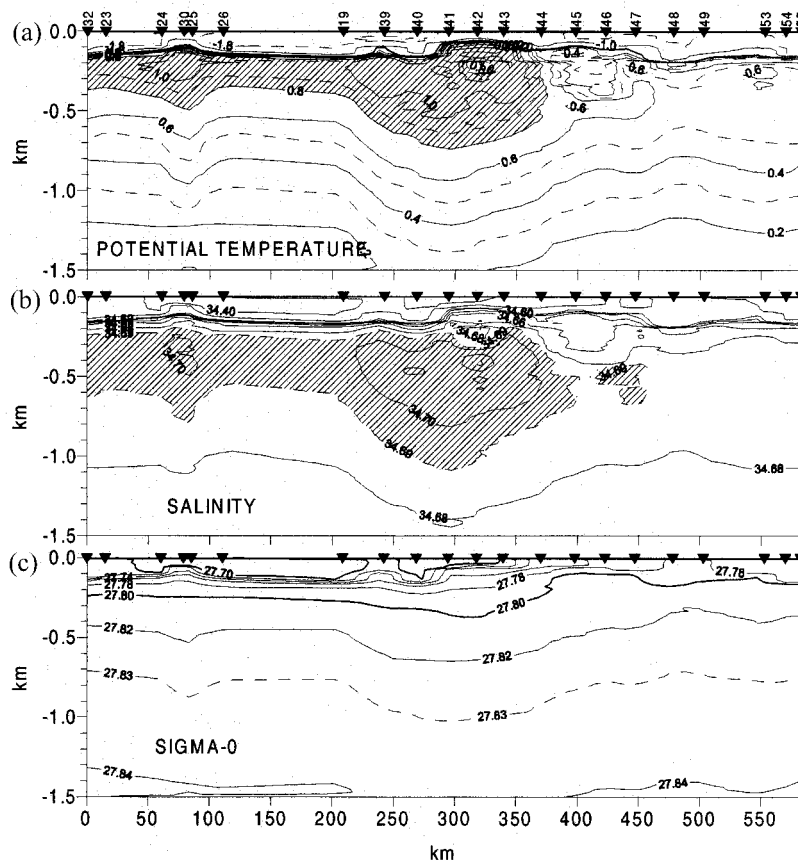


Figure 3. As for Figure 2 for the southernmost west-southwest to east-northeast regional shipboard transect 2. Maud Rise underlies the eastern (right-hand) end of the transect, and its steep western flank underlies stations 39–44.

mixed layer starts with the onset of sea ice formation, as brine released to the water column causes convection and erosion of the pycnocline. This entrainment leads to an increase in $\delta^3\text{He}$ and a decrease in DO concentration in the mixed layer during winter because gas exchange with the atmosphere is reduced by the ice cover.

3.2. Upper Ocean Features Associated With Maud Rise

The segments of the buoy drift along buoy sections I and II roughly paralleled ship transects 2 and 3 (Figure 1). (Note that Roman numerals refer to the buoy sections whereas Arabic numerals refer to the ship transects.) The major oceanographic features are apparent in both the ship's CTD and the buoy data. To emphasize the persistent features, we have averaged the shipboard CTD casts and buoy data together and interpolated over 0.05° longitude bins along the southern and northern transects (Plate 2 for northern section and Plate 3 for the southern section). Plates 2 and 3 show details of the T and S distributions from 0 to 150 m depth. To illustrate deviations from the average hydrographic conditions, Plates 2 and 3 also show the depth of the deepest temperature-conductivity sensor (sensor 3 at 155 m nominal depth) on the buoy and the differences between the temperature and salinity measured at that sensor (T_3 and S_3) and the average temperature and salinity gridded to that longitude and sensor depth ($\langle T_3 \rangle$, $\langle S_3 \rangle$). Bottom depth is shown underlying each of the combined sections.

The averaged buoy and ship data depict a similar and apparently continuous upper ocean structure between the northern and southern sections (Plates 2 and 3). The warm halo was present between 0.5°E and $1.5^\circ\text{--}1.7^\circ\text{W}$ along both sections and was associated with shoaling of the thermocline to depths as shallow as 65 m (Plates 2a and 3a). Less pronounced thermocline shoaling was present over the eastern and western inner flanks of Maud Rise, and the thermocline was slightly depressed over the center of the rise. Salinity was similarly distributed (Plates 2b and 3b), with both the halocline depth and the mixed layer S elevated over the central rise. The eastern boundary of the halo was less well defined in S than elsewhere. The saline core of the halo appeared slightly narrower than in the northern section, but this may have been due to closer sampling along the southern than along the northern section, with consequent tighter spatial resolution.

A shoaling of T and S isolines occurred along both sections between 5.7° and 7.5°W , about 270 km west of the halo. This feature may, if it was in fact continuous between the two sections, reflect larger-scale banding of the halo. Alternatively, it may not have been continuous between the northern and southern sections and may have reflected the presence of eddies shed from the circulation features associated with Maud Rise.

While the regional T and S features remained essentially unchanged over timescales up to months, the smaller-scale structures differed between the buoy and the ship-based CTD

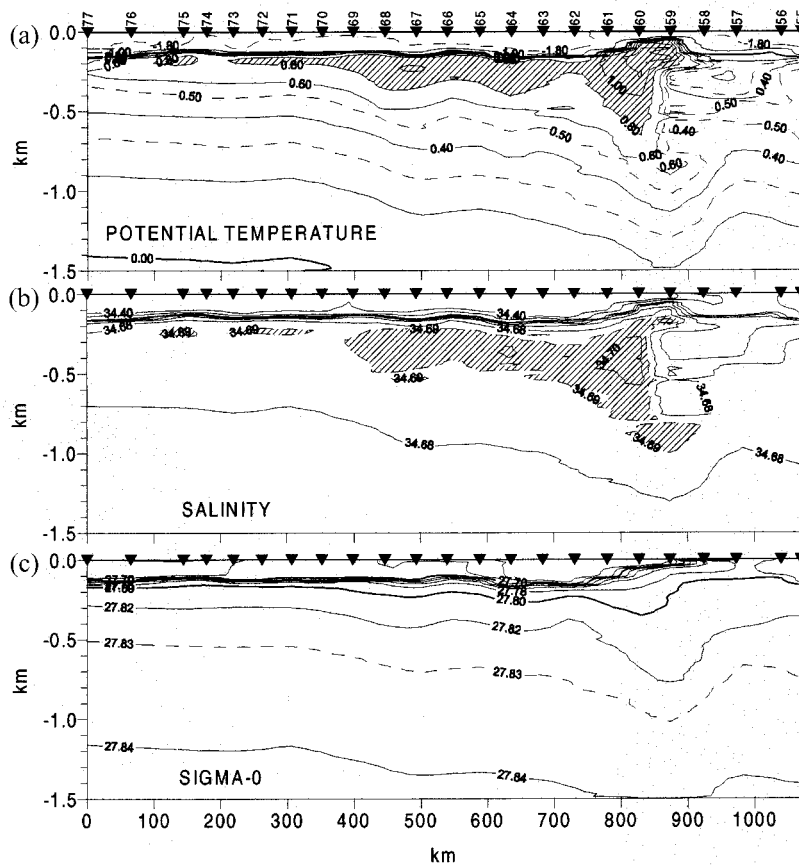


Figure 4. As for Figure 2 for the northernmost east-west regional shipboard transect 3. Maud Rise underlies the eastern (right-hand) end of the transect, and its steep western flank underlies stations 59–61.

data. Along the northern section the warm core of the halo appeared, based on $T3 - \langle T3 \rangle$ and $S3 - \langle S3 \rangle$ (Plate 3), to have bifurcated into two broad filaments at 3.2° – 1.6° W and 0.7° W– 0° . Between 1.6° and 0.7° W the instantaneous buoy data indicate anomalously cold, fresh conditions ($T3 - \langle T3 \rangle$ and $S3 - \langle S3 \rangle$ negative), and the buoy castlet in this band suggests that a gap was present in the halo structure. Conversely, the buoy indicates anomalously warm, salty conditions ($T3 - \langle T3 \rangle$ and $S3 - \langle S3 \rangle$ positive) at 3.2° – 1.6° W. The buoy data in this band indicate that the halo structure was present, though the ship-based CTD cast did not show the structure.

Similar features are evident along the southern section where the buoy and CTD data both show the narrow, low temperature gap in the halo near 1.0° W (Plate 2). The instantaneous anomalies $T3 - \langle T3 \rangle$ and $S3 - \langle S3 \rangle$ show that the buoy recorded substantial variability west of the halo. The buoy traversed the region between 1.5° and 2.5° W twice, once to the north and once to the south (Figure 1). The northern traverse detected warmer, saltier conditions than average, and the southern transit saw colder, fresher conditions. A warm-core feature was present about 40 km southwest of the halo between 2.9° and 3.7° W, and numerous small features were present between 4.5° and 7.5° W. East of the halo, the buoy encountered several small features with slightly elevated instantaneous T and S that may reflect either meridional or temporal variation in the halo boundary or eddy-like features that originated from the halo.

Numerous warm-core features populated the region west of

the halo in the southern section and are indicated by high T and S variability in the instantaneous buoy data $T3 - \langle T3 \rangle$ and $S3 - \langle S3 \rangle$. About 10 such features, varying in size from 5 to 20 km, were observed between 3.8° and 7.4° W. They bring warm water closer to the surface and allow substantial upward turbulent heat flux in areas where the heat flux would otherwise be small [McPhee *et al.*, 1999]. Their contribution will be further discussed below.

The above discussion describes the distributions of T and S along defined northern and southern sections; however, buoy data were obtained northeast of the northern section. These data (not shown) indicated that the halo did not extend significantly north of the northern section. Only a few warm-core features 20–30 km across, which we interpret as warm-core eddies, were observed along this northernmost portion of the buoy drift.

The combined ship-based and buoy data were used to construct spatial maps of T and S at 100 and 70 m depths (Plate 4). Various interpolation schemes were considered for this purpose, and it was concluded that linear interpolation was adequate given the data coverage and the desire to provide a reasonable conceptualization of the conditions. The halo appears as an elliptical 60 by 150 km warm (1.25°) high S (34.7 psu) pool over the southwest slope of the rise. The pool tapered at its northern and southern ends, but since no data were obtained north-northeast of the rise, it was not possible to determine the extent of the halo in that direction. The halo was better defined at 70 m than deeper and showed the greatest

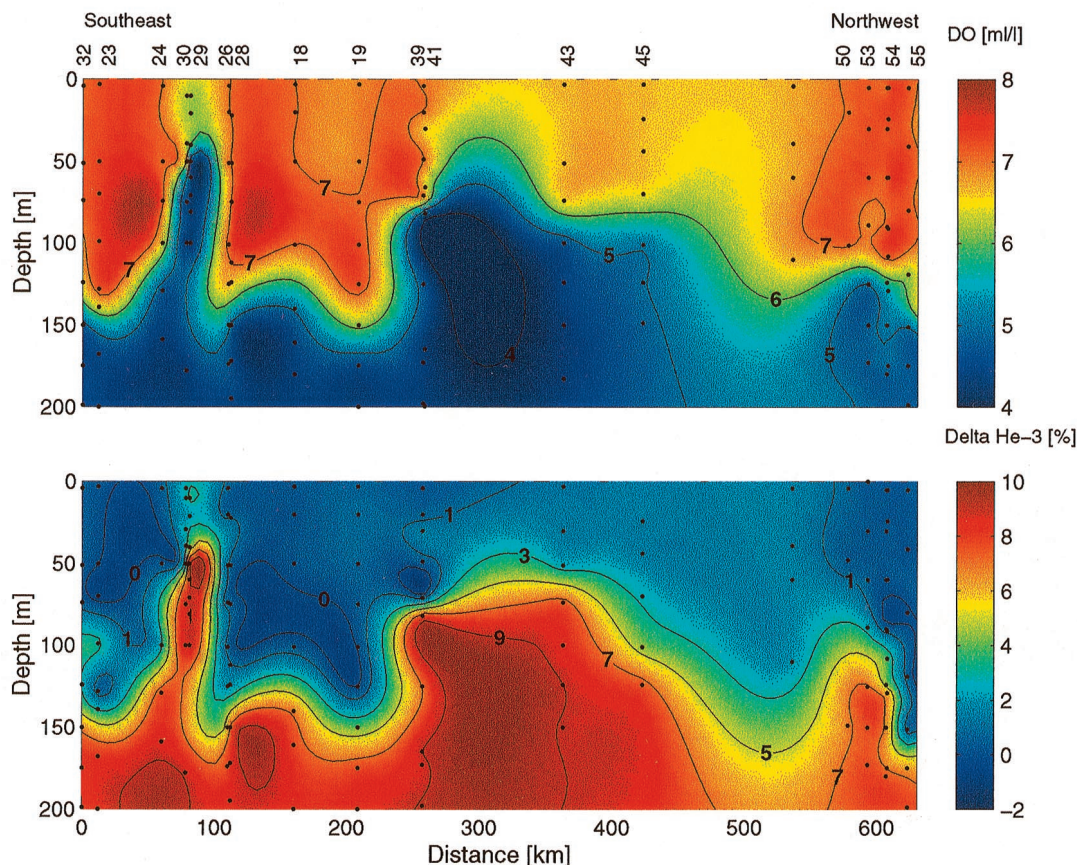


Plate 1. Distribution of (top) DO and (bottom) $\delta^3\text{He}$ in the upper 200 m along shipboard transect 2. Dots indicate locations of the bottle data. Maud Rise underlies the right-hand end of the section.

upbowing of isolines over the southwest margin of the rise (Plates 4c and 4d). The bifurcated structure of the southern portion of the halo is apparent (Plates 4a and 4b). The detached warm-core feature, described relative to the northernmost section of the buoy drift, is evident near 64.7°S , 2.5°W (Plates 4a–4d).

Vertical ADCP current profiles were measured during each of the two drifting stations and were used to compute mean upper layer (50–300 m) currents. At the first site, in the warm regime the upper layer moved southwestward at about 3 cm s^{-1} . Mean upper layer flow during the second drifting station, over Maud Rise, was about 2 cm s^{-1} southwestward. Each of these records is about 6 days long and is subject to bias from local and variable mesoscale activity and long-period tides. The measurements over eastern Maud Rise indicated that weak vertical shear observed across the pycnocline was due primarily to semidiurnal band processes, probably either tides or near-inertial oscillations.

It is not possible to collect hull-mounted ADCP data from a vessel that is underway in sea ice because ice particles and bubbles interfere with the acoustic signal. ADCP data were, however, obtained during the CTD stations that were taken apart from the drift sites. These data records were 2–3 hours in length and were too short in duration, relative to tidal time-scales, to allow computation of statistically significant mean currents. Two of these short-current time series did, however, show south-southwest upper layer mean speeds $O(10)\text{ cm s}^{-1}$ associated with the halo over the western flank of the rise,

exceeding the regional tidal current speeds by a factor of 2. For comparison, south-southwest currents having speeds of $4\text{--}5\text{ cm s}^{-1}$ were reported by Bersch *et al.* [1992] in the region of the halo southwest of the rise. Results from the $1/4^\circ$ Parallel Ocean Climate Model (POCM 4B) [Semtner and Chervin, 1992; Stammer *et al.*, 1996], described in greater detail below, indicate long-term mean southwestward regional current speeds of $2\text{--}3\text{ cm s}^{-1}$.

The tracer distributions, despite their relatively limited horizontal resolution, reinforce our description of the main features associated with Maud Rise (Plate 1). Southwest of the rise, the halo and warm pool region coincides with a region of high $\delta^3\text{He}$ (1.2–1.7%) and low DO ($6.5\text{--}6.7\text{ mL L}^{-1}$) values in the winter mixed layer (stations 41, 43, and 45). Unfortunately, no tracer data are available at station 42, where T data suggest the presence of either a cold band separating two warm halo filaments or a cold subsurface core.

A warm-core feature ($T > 1.0^\circ\text{C}$) between 100 and 200 m was centered on transect 1 about 50 km from its southern end. The isopycnals show a cyclonic baroclinic circulation associated with the feature, consistent with the presence of an eddy. The thermocline directly over the core of this feature was elevated to within 40 m of the surface, and the upper layer T above the warm core of this feature was elevated to more than -1.25°C , compared with upper layer temperatures below -1.8°C in the surrounding area. A DO concentration of $6.1\text{--}6.3\text{ mL L}^{-1}$ and very high $\delta^3\text{He}$ values of 2.7–3.1% were observed in the winter mixed layer at stations 29 and 30. The

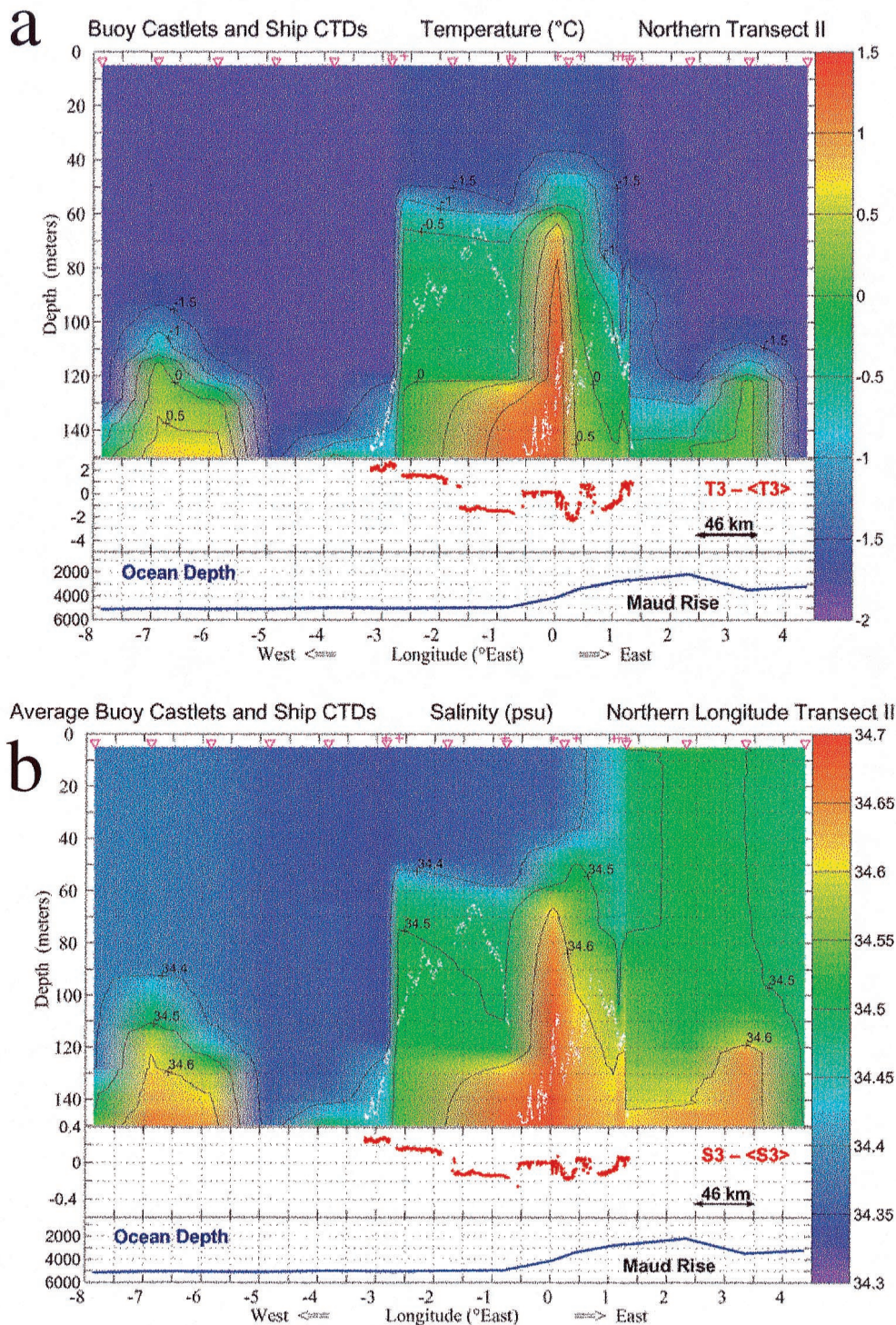


Plate 2. Distributions of upper ocean (a) T and (b) S as functions of depth and longitude constructed using averaged T and S data from northern buoy section II and CTD data from the eastern part of shipboard transect 3. Contour intervals are 0.5°C for T and 0.1 for S . White dots show the maximum depths sampled. Deviation between T (or S) measured by the deepest buoy sensor (nominal depth of 155 m) and averaged T (or S) at the same depth is shown on the middle panel. Underlying seafloor topography is shown on the bottom panel. Locations of the vertical sensor excursions (see text) and CTD stations are also indicated.

chemical and tracer properties measured within the cell are similar to those found in the warm pool at stations 42 and 43, consistent with its location in the warm pool following advection downstream from the halo. A more detailed description of

this eddy is provided by *McPhee et al.* [1996]. Similar features were present near the same site about 100 km from the western end of transects 2 and II (Figure 3), and also near the center of transect 3 (Figure 4). The core T and S properties of these

features identify them as similar to waters in the Maud Rise halo, and we presume that being downstream from the halo, they were at one time associated with it.

4. Discussion

4.1. The Taylor Column Conceptualization

The hydrographic structure that is associated with Maud Rise can be characterized as deriving from a Taylor column centered atop the rise. A Taylor column can be simplistically described as follows. A steady current impinges on an isolated topographic feature such as a seamount. The fluid column is compressed vertically on the upstream side of the feature and stretched on the downstream side, producing anticyclonic and cyclonic vortices that corotate about the seamount. If sufficiently strong, the steady current will flow over the seamount and sweep both vortices downstream. A weak current will carry the cyclonic vortex downstream; however, the anticyclonic vortex remains trapped atop the seamount as a Taylor column. The region of fluid trapped inside the column is known as a Taylor cap.

A model of flow past a seamount by *Goldner and Chapman* [1997] incorporates both Taylor column formation and the residual peripheral circulation associated with impinging deep-ocean tidal flows. They applied their model to Fieberling Guyot. Their results are, however, intended to have considerable generality and can be applied with some confidence to the Maud Rise case. To this end a number of external parameters for the two cases may be compared. Incident mean current strength is expressed in terms of the Rossby number $R_0 = U/fL$, where U is the incident current speed, f is the Coriolis parameter, and L is the horizontal length scale of the feature. A Taylor column can be expected to form when $R_0 \ll 1$. For Fieberling Guyot, $R_0 = O(10^{-2})$ [Brink, 1995] so that a Taylor column was formed. Maud Rise is broader than Fieberling Guyot, about 100 km compared to 20 km. The observations presented in section 3.2 suggest a mean inflowing current speed of 1–2 cm s^{-1} . The resulting Rossby number for Maud Rise is then $R_0 = O(10^{-3})$; thus we expect a Taylor column to form. Fieberling Guyot extends farther up in the water column than Maud Rise. As *Goldner and Chapman* [1997] point out, however, a number of recent models have suggested that in the case of small R_0 a Taylor column will form over a broad range of seamount heights. Finally, stratification as expressed by N is about a factor of 5 stronger at Fieberling Guyot than over Maud Rise. We expect weaker stratification to facilitate formation of a Taylor column, whereas stronger stratification would tend to decouple upper layer flow from the deeper circulation.

Tidal currents impinging on Maud Rise probably generate slope-trapped peripheral mean currents. In the case of Fieberling Guyot, impinging tidal currents having speeds $U_t \approx 0.3 \text{ cm s}^{-1}$ were amplified over the seamount by 50–100 times when seamount-trapped waves were excited [Goldner and Chapman, 1997]. A mean rectified current $O(10) \text{ cm s}^{-1}$ was generated that flowed anticyclonically around the seamount rim. Deep ocean tidal currents impinging on Maud Rise have been determined both from the current data referred to above and from a recent tidal model [Robertson et al., 1998] to be 1–2 cm s^{-1} . Measurements made using the hull-mounted ADCP during the ANZFLUX experiment, and results from this model show tidal current amplitudes of $O(5) \text{ cm s}^{-1}$ over the rise. The pertinent parameter in the *Goldner and Chapman*

[1997] model, U_t/fL , was varied over a range given as 1.1– 5.6×10^{-3} . For Maud Rise, $U_t/fL = 7.5 \times 10^{-4}$ – 1.5×10^{-3} , at or below the low end of the range of values for Fieberling Guyot. On the basis of this model we expect that a Lagrangian mean tidal residual flow of $O(1) \text{ cm s}^{-1}$ should be present over the cap of Maud Rise. Similar residual current speeds were reported by *Padman et al.* [1992] for the Yermak Plateau, a topographic rise in the eastern Arctic Ocean that has many similarities to Maud Rise. However, the predicted rectified Eulerian currents decrease rapidly as water depth increases; thus the tide-induced circulation is too small to be observed from the shipboard ADCP. Any rectified tidal circulation would be anticyclonic and would augment that flow due to the Taylor column dynamics. As noted above, both our short-term observations and the 8-month means reported by *Bersch et al.* [1992] show current speeds of 2–5 cm s^{-1} in an anticyclonic sense along the 4000–4500 m isobath on the western flank of the Rise. Mean current speeds did not vary significantly between about 1000 m depth and near-bottom in the *Bersch et al.* [1992] data, which presumably incorporate both the Taylor column and tidal rectification effects.

These results provide us with new kinematic and dynamic perspectives from which to interpret our field data. The halo overlying the rise and the warm pool to the southwest are both consistent with the presence of a Taylor column overlying Maud Rise [e.g., *Ou*, 1991; *Bersch et al.*, 1992]. Recent numerical model results are consistent with the foregoing. To demonstrate this, Lagrangian particle tracks based on predicted currents from POCM 4B [Semtner and Chervin, 1992; Stammer et al., 1996] in the region of Maud Rise are shown in Figure 5. For this exercise we tracked particles in model level 8 (layer middepth of 310 m, roughly at the WDW maximum T), using the annual averaged model velocity field for 1994. We used bicubic splines for interpolation. At each time step we calculate the advection based on velocity at the previous time step, then recalculate the advection using the average of the interpolated velocities at the initial and final positions for that time step. The POCM 4B run was initialized from fields taken from a previous model run covering a spin-up of over 40 years from *Levitus* [1982] hydrography. The model incorporates the *Barnier et al.* [1995] heat flux climatology, in addition to relaxing the surface T and S fields to the *Levitus and Boyer* [1994] and *Levitus et al.* [1994] climatology with a 30 day relaxation timescale. Thus the velocity field is not entirely independent of the pre-ANZFLUX hydrographic database in this region. There is no sea ice in this version of POCM, so that any effect of ice on the penetration of wind stress into the ocean interior is not considered. *Wamser and Martinson* [1993] found that on the average, ice cover in the eastern Weddell Sea lowered the air-sea momentum flux by about a third. Given the particularly thin and mobile nature of the regional pack ice that we observed during the ANZFLUX experiment, neglect of the ice cover probably does not significantly impact our results. The tracks show qualitatively what we expect from the ANZFLUX hydrography. The inflow of CDW and WDW westward past Maud Rise bifurcates just east of the rise, consistent with an estimate by *Fahrbach et al.* [1998] that 14 Sv flows to the north and 4 Sv to the south of the rise. (Their estimate excluded the ACC that is trapped along the coastal continental shelf and slope to the south of the rise.) Some of the northern branch, however, enters the Taylor column circulation southwest of the rise and recirculates clockwise around the center of the rise (see the track originating at 64.5°S, 10°E in Figure 5). In this

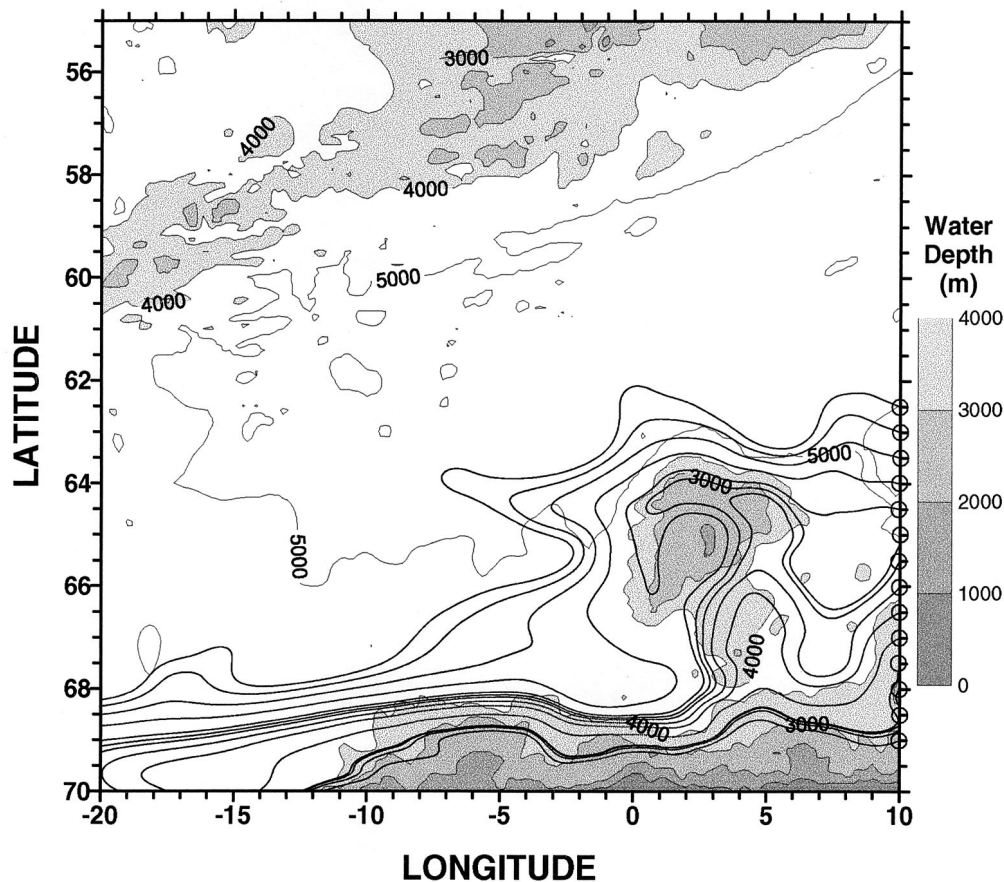


Figure 5. Lagrangian particle tracks from the Parallel Ocean Climate Model based on annual averaged mean flow for 1994 for the layer centered at 310 m. Open circles along 10°E show the initial positions of each particle. See text for details.

Lagrangian view the warm pool appears as the region southwest of Maud Rise consisting of water that has traveled around the northern edge of the rise. The term warm pool connotes a somewhat quiescent feature. If we view it, however, as a region, even though poorly defined, of mean cyclonic vorticity, then it follows that dynamics within this region favor upward doming isopycnals and isotherms and a larger-scale clockwise recirculation. Finally, we note that the depicted trajectories result from time-averaged model results that include mesoscale fluctuations. These trajectories are consistent with what appear to be permanent oceanographic features, and we interpret this to mean that the mean flow exerts a strong control over these features.

While the presence of a Taylor column tends to isolate the waters in the immediate vicinity of Maud Rise, the waters of the broader area surrounding Maud Rise are also somewhat isolated relative to the rest of the interior Weddell Gyre (D. G. Martinson and R. A. Iannuzzi, Spatial/temporal patterns in Weddell Gyre characteristics and their relationship to global climate, submitted to *Journal of Geophysical Research*, 2000, hereinafter referred to as Martinson and Iannuzzi, submitted manuscript, 2000). This is apparent from the results of an empirical orthogonal function (EOF) analysis of robust upper ocean property distributions that characterize climatically relevant aspects of the ocean-atmosphere-ice (OAI) system (see Martinson and Iannuzzi [1998], for derivations, descriptions

and climatologies). The EOF analysis is part of the optimal analysis (OA) technique of Kaplan *et al.* [1998], which Martinson and Iannuzzi (submitted manuscript, 2000) employ to overcome analysis impediments imposed by the sparse and sporadic distribution of historical ocean data throughout the Weddell Gyre region. The OA technique requires the estimation of a covariance matrix that describes the covariability of features across the gyre. This is then decomposed into EOFs, and the lowest-order EOFs serve as the basis for interpolation of the sparse data onto a regular grid in space and time. Analysis of the coherent spatial structure in each mode reveals that the lowest two modes are dominated by interannual variability along the northern rim of the gyre. Variability in the central gyre, including the Maud Rise region and the northwestern rim of the gyre, dominates the third mode (Plate 5b), which includes 5–20% of the variance.

The modes (represented by the principal components) show that the strongest temporal covariability in bulk property parameters is associated with extrapolar El Niño–Southern Oscillation (ENSO) climate variability (Martinson and Iannuzzi, submitted manuscript, 2000). The correlation coefficient of this covariability exceeds 0.9 in the eastern Weddell Sea. Further examination shows that this variability is associated primarily with changes in mixed layer salinity and in the depth and temperature of the WDW. Changes observed specifically in the Maud Rise region (Plate 5a) show a very strong covariability

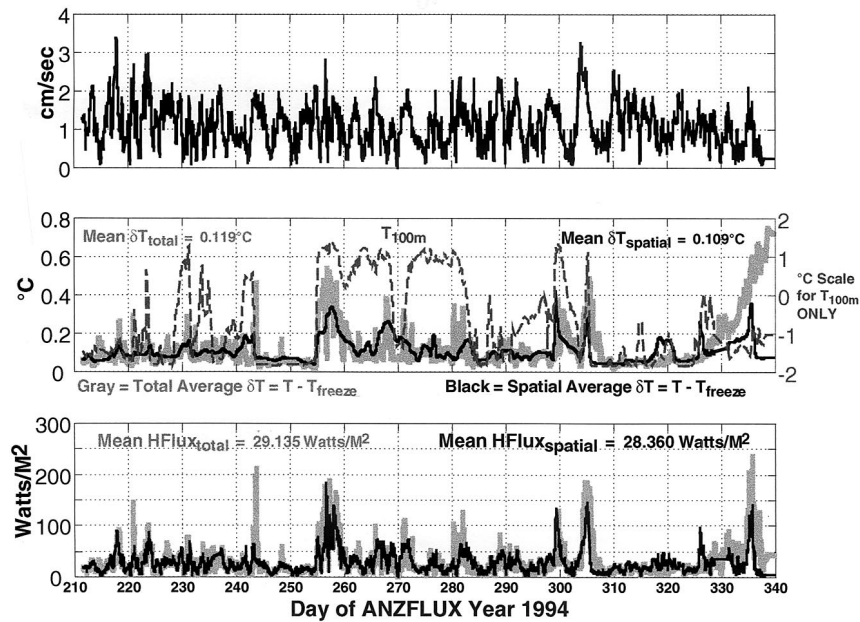


Figure 6. Heat flux parameters during the buoy drift with (top) u^* computed according to the *McPhee et al.* [1998] relationship to drift speed, (middle) δT equal to the elevation of the 10 m temperature above freezing, and (bottom) the resultant heat flux computed using $C_H = 0.0056$. T at 100 m depth, interpolated to the buoy position from the ship CTD and buoy castlet averages, is also shown.

with ENSO ($r = 0.94$ for bulk stability, significant to within 1%; $r^2 > 85\%$), consistent with enhanced winter cyclonic forcing during El Niño and diminished forcing during La Niña conditions. These changes may reflect shifts in winter storm tracks. Analysis of the Goddard Institute of Space Studies (GISS) general circulation model (D. Rind et al., Latitudinal temperature gradients and sea ice response, submitted to *Journal of Geophysical Research*, 2000) reveals a mechanism wherein warm anomalies in the tropical Pacific increase the equatorward thermal gradient, invigorate the subtropical gyre, and shift the subtropical jet equatorward away from the source of available potential energy in the Antarctic. This leads to a decrease in cyclone activity in the Pacific sector of the subtropical oceans. The equatorial warming also alters the Walker cell circulation, leading to a reduction in subsidence in the tropical Atlantic. This reduction in turn alters the vertical meridional circulation in the Atlantic, introducing changes comparable to those that would occur were the tropical Atlantic to cool and create a meridional temperature gradient opposite in sign to that in the Pacific. This results, in the Atlantic, in a relaxation of the meridional circulation accompanied by a poleward shift of the subtropical jet to a location nearer the Antarctic potential energy sources. The result is increased storm intensity in the Atlantic sector of the Southern Ocean and increased energy input to the Weddell Gyre, consistent with the findings here.

4.2. Heat Fluxes

A primary motivation for the ANZFLUX experiment was to determine the ocean heat flux to the surface and its relation to the regional oceanography. Modeling studies [e.g., *Martinson*, 1990] have indicated that maintenance of the relatively thin Weddell Sea ice cover requires heat fluxes $O(10\text{--}20) \text{ W m}^{-2}$. Observations of ice growth, elevation of T above freezing, and entrainment of geochemical tracers have tended to be consis-

tent with these values for the Weddell Sea [*Wadhams et al.*, 1987; *Gordon and Huber*, 1984, 1990; *Schlosser et al.*, 1990]. The appearance of the Weddell Sea winter polynyas in the mid-1970s occurred in the vicinity of Maud Rise and suggest that it may be an area of particularly large heat flux.

During the ANZFLUX experiment, *McPhee et al.* [1999] measured instantaneous heat fluxes at the drift stations in the warm pool and over Maud Rise (site locations shown schematically on Figure 1) and found that average fluxes in these regions were 52 and 23 W m^{-2} , respectively. They also derived parametric relations among heat flux, ice drift speed, and water temperature in the form $\langle w'T' \rangle = C_H u^* \delta T$, where $\langle w'T' \rangle$ is the turbulent heat flux, u^* is the friction velocity related to (and roughly proportional to) the velocity of the ice over the water, δT is the elevation of the mixed layer temperature above the freezing point, and C_H is the heat transfer coefficient. They found that u^* could be determined from the ice drift velocity using a Rossby similarity relationship with parameters similar to those for the Arctic pack ice if a roughness scale ($z_0 = 1\text{--}2 \text{ mm}$) 2 orders of magnitude smaller than that in the Arctic was assumed for the Weddell Sea ice. The heat transfer coefficient was found to equal 0.0056, a value within 10% of Arctic pack ice values. These measurements were carried out over a range of conditions that appeared to typify the region during winter. These relationships were used with the POP buoy drift speed and the temperature elevation above freezing at the 10 m sensor to estimate the heat flux over the first 76 days of the buoy drift, yielding an areal average flux of 27 W m^{-2} .

McPhee et al. [1999] showed precisely how large the ocean heat flux could be and how to calculate it on the basis of local conditions. We expand upon their work by exploring variations in the heat flux with regional ocean conditions. We start by considering variations in pertinent heat flux parameters during

Table 1. Buoy and $\delta^3\text{He}$ Heat Flux Statistics by Region

Drift Region	Average Q , W m^{-2}	Average u^*	Average δT	Average T_{100}	Correlations $u^*/\delta T$	Correlations Q/T_{100}	Correlations $Q/\delta T$	Correlations Q/u^*	$\delta^3\text{He}$ Q , W m^{-2}
Warm pool	27.5273	1.3477	0.0867	-0.9049	-0.0120	0.0771	0.4919	0.7594	25
South halo	23.0996	0.9809	0.1011	-0.1640	-0.0671	0.2500	0.6016	0.6767	25
Cold pool 1	17.9891	1.1149	0.0617	-1.3054	0.3312	0.7213	0.7482	0.5108	15
Central halo 1	44.6306	1.0768	0.1878	0.3535	-0.2067	0.3249	0.6027	0.4185	25
Maud Rise 1	10.9714	0.6647	0.0694	-1.0632	0.2258	0.2473	0.1516	0.9902	20
Central halo 2	27.9036	1.0254	0.3547	0.4790	0.1607	0.0399	0.3338	0.6049	25
Maude Rise 2	20.0405	1.1020	0.0765	-1.0220	0.0302	0.5109	0.7157	0.7177	20
North halo	24.2808	1.0338	0.1107	-0.5278	-0.3307	0.5387	0.8460	0.4402	15
Warm feature	81.9601	1.8101	0.2054	0.1445	-0.2774	0.6271	0.8548	0.2514	
Cold pool 2	14.2326	1.1538	0.0563	-1.3232	-0.3723	0.0213	0.6000	0.5635	15
No MIZ drift	26.6923	1.1299	0.1019	-0.5433	-0.0508	0.4297	0.7682	0.4801	
MIZ	53.4908	0.8543	0.2884	-1.0912	-0.2730	-0.1176	-0.2026	0.4698	
Whole drift	29.1352	1.1047	0.1190	-0.5934	-0.1397	0.3054	0.7320	0.4034	

MIZ, marginal ice zone.

the buoy drift track (Figure 6). Maximum upward flux occurred over the halo and was nearly 200 W m^{-2} , while the flux averaged over the whole drift was 29 W m^{-2} . This average is higher than that reported by *McPhee et al.* [1999] because it includes the high heat flux periods near the end of the record (after day 325) when the buoy neared the ice edge.

To assess the relations among heat fluxes and regional oceanographic features, the data were divided into bins for each region through which the buoy passed. Average heat fluxes in these bins were derived using T elevation above the freezing point at 10 m measured from the gridded ship CTD and buoy castlet averages (Plate 6 and Table 1). The value for u^* that was calculated from the buoy record (Figure 6) was assumed to represent the u^* history of the region and was used in the heat flux calculation. Heat fluxes were smallest ($14\text{--}18 \text{ W m}^{-2}$) in the relatively cold region west of the halo, north of the warm pool, and overlying Maud Rise ($11\text{--}20 \text{ W m}^{-2}$). They were intermediate in the northern and southern halo ($23\text{--}24 \text{ W m}^{-2}$) and in the warm pool (28 W m^{-2}) and were highest ($24\text{--}45 \text{ W m}^{-2}$) in the central halo, in the marginal ice zone near the northern ice edge (54 W m^{-2}), and in an isolated warm feature (82 W m^{-2}). Heat fluxes even from the coldest regions were substantial.

A key question is whether the heat flux is constrained by the availability of heat in the ocean or by the intensity of mechanical mixing. The correlation coefficients (Table 1) yield a partial answer. The record-long correlation of heat flux with T elevation (0.73) was greater than that with friction velocity (0.40), where correlations >0.3 were significant at the 95% level. The correlation between heat flux and 100 m temperature, taken to be an indicator of independent thermal forcing, was lower still (0.31). Hence heat entrainment through the thermocline by mechanical mixing was not significantly enhancing the thermal forcing. The correlation between u^* and T elevation at 10 m was near zero. The average heat flux of 29.1 W m^{-2} nearly equaled, throughout the study region, the 30.8 W m^{-2} obtained as a product of the average values of u^* and temperature elevation [*McPhee et al.*, 1999].

Fluctuations in heat flux and T at 100 m were less correlated in regions of high flux. The correlation was 0.72 in the cold region west of the rise, where heat flux was 18 W m^{-2} , but was only 0.32 in the central halo, where heat flux was 45 W m^{-2} . These differences are probably due to the regionally varying mixed layer depth. Many instances of elevated mixed layer T and consequent high heat fluxes associated with warm patches

in the mixed layer resulted from entrainment of warmer deep water during past storm events. These warm patches were more numerous over the halo than elsewhere because of the shoaled thermocline, with the result that the average T elevation was high. There were fewer warm patches in the colder regions, average T elevation was less, and a greater proportion of the heat flux was associated with the warm patches.

An evaluation of upper ocean DO and $\delta^3\text{He}$ balances in ice-covered regions of the ocean provides an alternate means by which to assess heat fluxes through derivation of entrainment rates. This method is based on the observation that DO is undersaturated by about 20% and has little variation within the WDW [e.g., *Gordon and Huber*, 1990], whereas ^3He is supersaturated in the WDW [*Schlosser et al.*, 1987]. Gas exchange between the upper ocean and atmosphere is strongly reduced by the sea ice cover, therefore entrainment of WDW results in an increased concentration of $\delta^3\text{He}$ and a decrease in DO in the upper mixed layer. Compared to direct measurements of the vertical oceanic heat flux, which typically yield short time series with limited spatial resolution [e.g., *McPhee et al.*, 1999], the values derived from gas balances represent larger regions over periods of time from months up to a year. The method has been used previously to determine winter entrainment and heat flux rates for the Weddell Sea interpolated over large areas [e.g., *Gordon and Huber*, 1990; *Schlosser et al.*, 1987; *Hohmann et al.*, submitted manuscript, 2000].

The horizontal distributions of the vertically averaged mixed layer $\delta^3\text{He}$ and DO concentrations in the Maud Rise region during the ANZFLUX experiment reflect the features that are associated with Maud Rise (Figure 7). The halo and warm pool on the western flank of the rise as well as the warm cell at the south end of shipboard transects 1 and 2 stand out as regions with high mixed layer $\delta^3\text{He}$ values and low DO concentrations. The spatial coverage of the measurements is not sufficient to resolve entirely these features, and their dimensions in Figure 7 result primarily from linear interpolation of the data. Nevertheless, the data illustrate that the influence of the Taylor column on mixed layer $\delta^3\text{He}$ and DO does not extend into the region northwest of Maud Rise.

If we assume that the elevated $\delta^3\text{He}$ concentrations and low DO in the upper mixed layer result primarily from WDW entrainment and that sea-air gas exchange is strongly suppressed by the ice cover, then the apparent WDW fraction in the mixed layer can be computed using a two-component mixing approach. For this computation we now assume that WDW

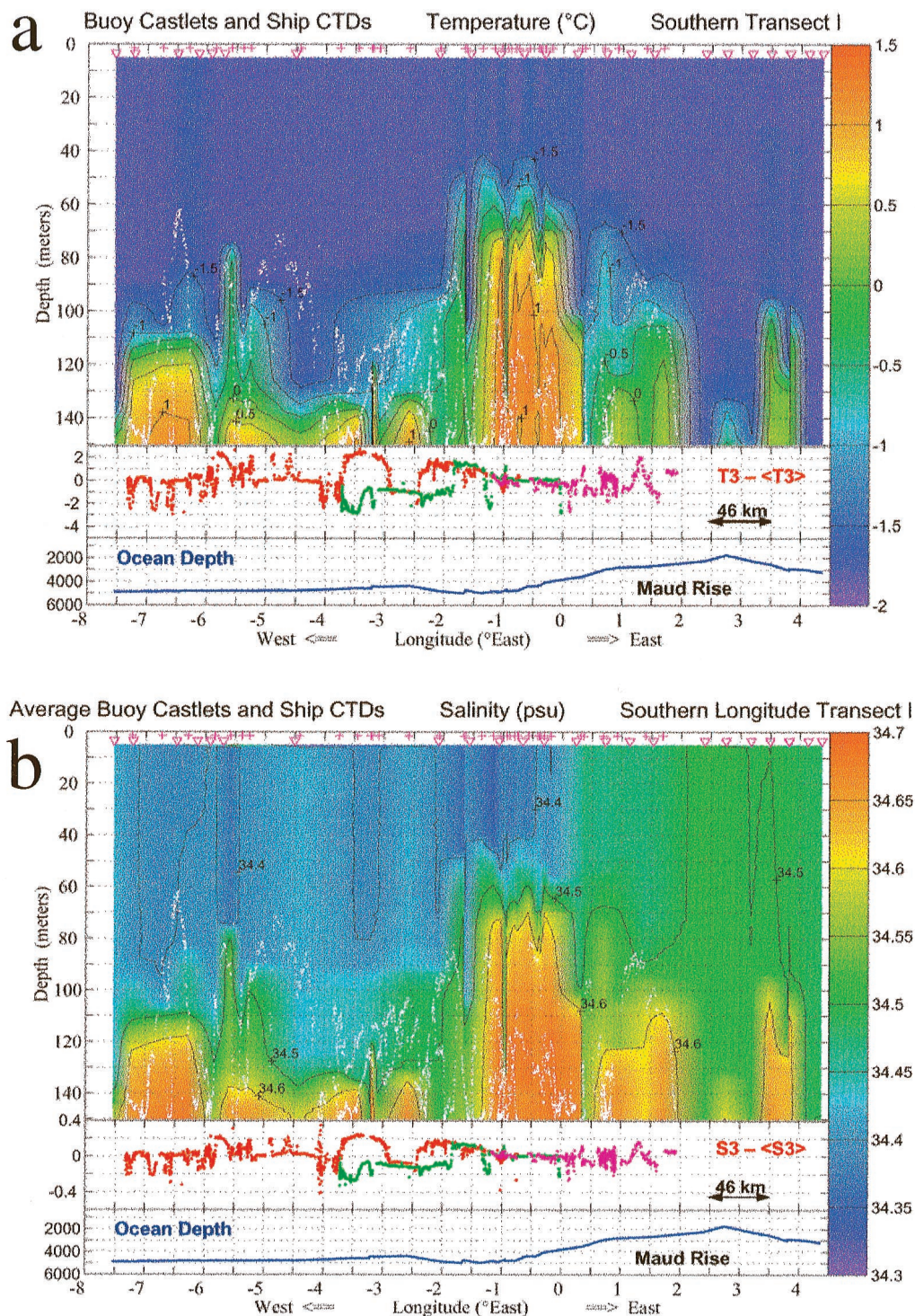


Plate 3. As for Plate 2 except along averaged southern buoy section I and shipboard transect 2.

at the depth of Θ_{\max} best represents that entrained into the mixed layer and use the corresponding values of $\delta^3\text{He}$ concentration = $8.6 \pm 0.2\%$ and $\text{DO} = 4.49 \pm 0.07 \text{ mL L}^{-1}$ for the deep mixing component. The initial mixed layer $\delta^3\text{He}$ concentration and DO at the onset of freezing were reported by Hohmann et al. (submitted manuscript, 2000) to be $-1 \pm 0.3\%$ and $7.67 \pm 0.11 \text{ mL L}^{-1}$, respectively. The latter value is at $92.4 \pm 1.4\%$ saturation for $\Theta = -1.87^\circ\text{C}$, $S = 34.3 \text{ psu}$, and $P = 990 \text{ mbar}$ [Weiss, 1970]. In the warm pool and the warm

cell or eddy southwest of Maud Rise the WDW fraction of the mixed layer derived from the $\delta^3\text{He}$ data turns out to be about 30 and 45%, respectively, which is a factor of 2–3 higher than in other regions covered by the ANZFLUX cruise (Hohmann et al., submitted manuscript, 2000). Values obtained from DO are slightly lower, probably because the effect of primary production on DO has been neglected.

Rates of entrainment of WDW into the mixed layer are computed using the measured WDW fractions in the mixed

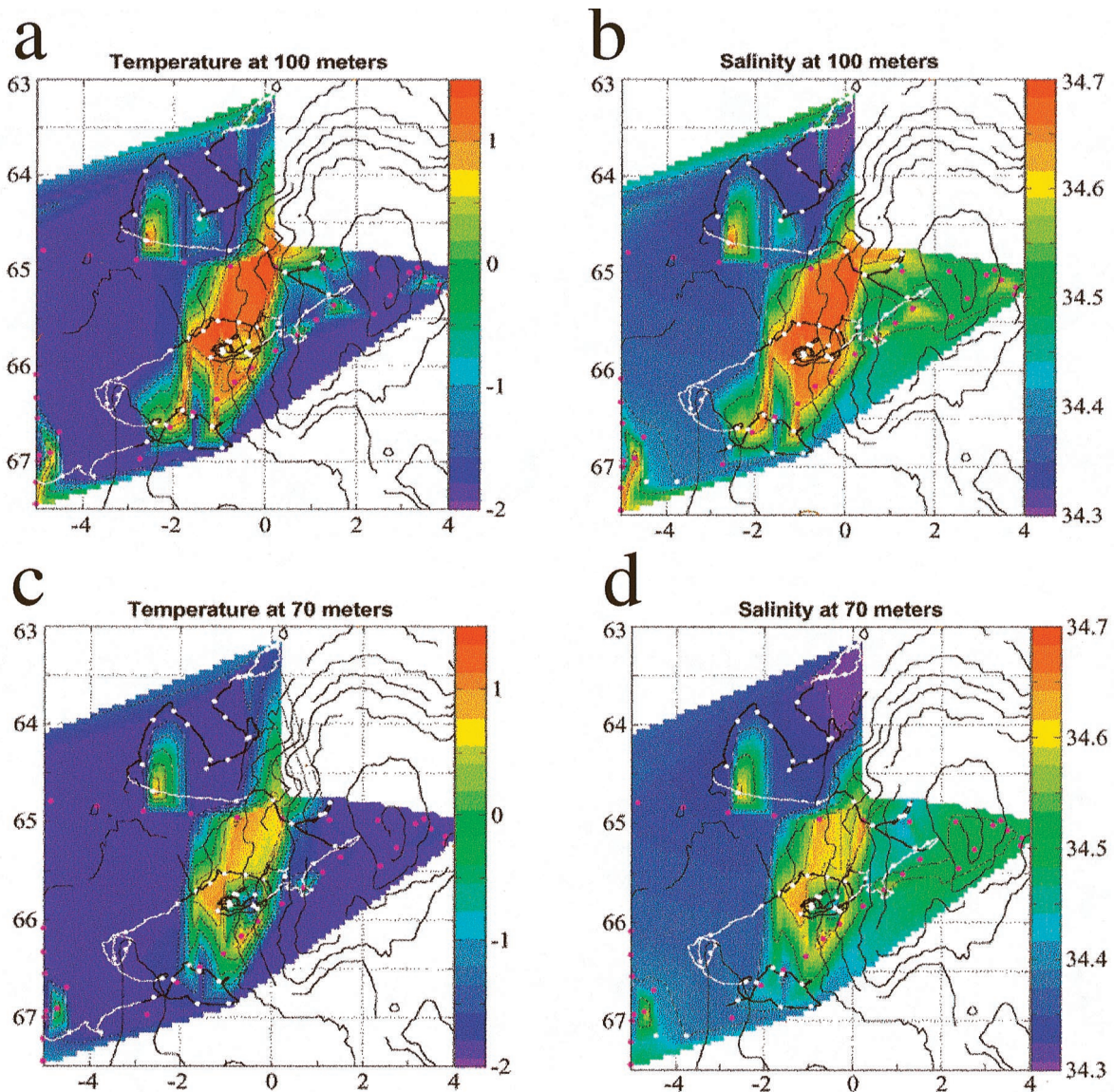
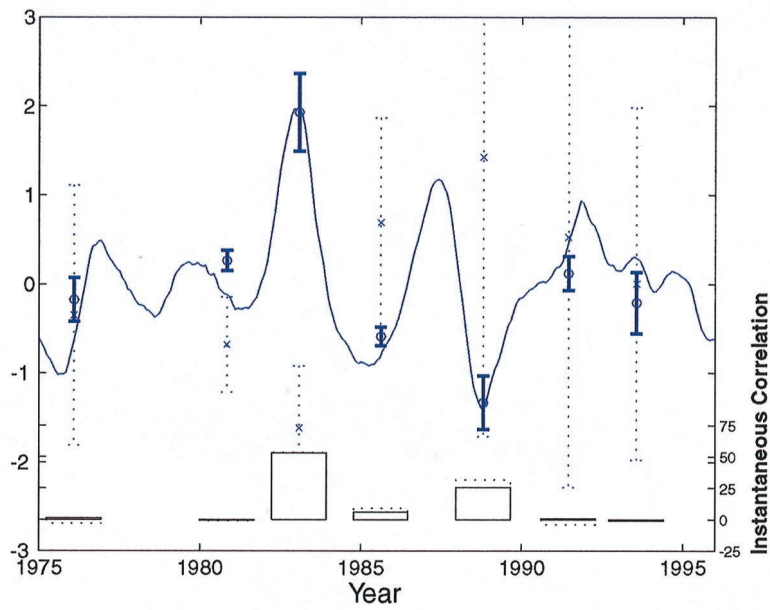


Plate 4. Distributions of T and S at (a) and (b) 100 m and at (c) and (d) 70 m based on the combined and bin-averaged buoy castlet and ship's CTD data. Colored dots show the shipboard CTD station locations, and white dots indicate locations of buoy castlets.

layer, mixed layer depth, and time elapsed since formation of the sea ice cover. If we assume that the ice edge progresses northward at a constant rate, then the time when each site becomes ice-covered can be estimated using a linear correlation between the time of first ice formation, derived from National Snow and Ice Data Center (NSIDC) data [Schweitzer *et al.*, 1995], and latitude at the site. The entrainment heat flux at each site is the product of entrainment rate, T difference between the WDW and the mixed layer, density, and specific heat of seawater.

Using $\delta^3\text{He}$, the greatest winter heat fluxes (about 25 W m^{-2}) were found in the warm pool and the warm cell or eddy southwest of Maud Rise (Figure 8 and Table 1). Note that the greatest flux was found at station 28, rather than at 29 and 30, though these latter two sites had the highest $\delta^3\text{He}$ and lowest DO values in the mixed layer, and this apparent discrepancy reflects the difference in mixed layer depth between the sites.

The 25 W m^{-2} value for heat flux derived at station 28 using $\delta^3\text{He}$ is considerably lower than the 100 W m^{-2} that was directly measured at the same site by McPhee *et al.* [1996], but the latter is an instantaneous value, while the fluxes derived using $\delta^3\text{He}$ reflect time-integrated processes. Elsewhere in the region, typical values of winter entrainment heat flux derived from $\delta^3\text{He}$ are about 15 W m^{-2} . If we incorporate the higher values that were associated with the halo and warm eddy, then the regional values were similar to but slightly lower than the $27\text{--}29 \text{ W m}^{-2}$ regional mean derived from the drift buoy data. There are two possible reasons for this discrepancy. First, the buoy spent a large proportion of its drift situated in the warm pool and halo regions and therefore sampled preferentially from the highest heat flux regions. Second, the estimates based on $\delta^3\text{He}$ include fluxes averaged since the onset of sea ice formation, whereas the buoy values represent midwinter conditions encountered during the drift.



(Third EOF)

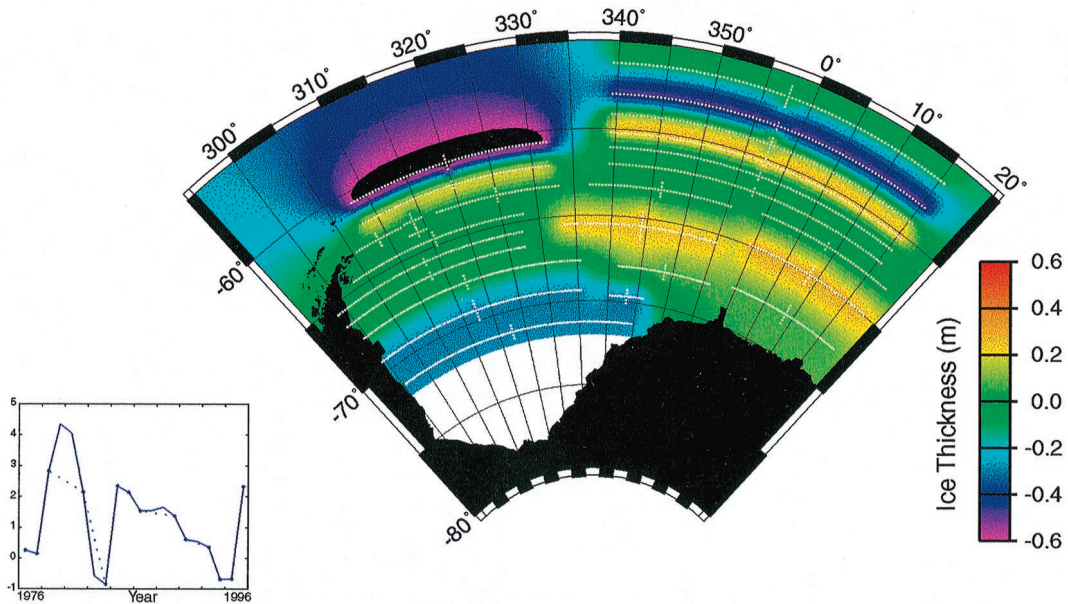


Plate 5. (a) Time series of NINO3 (an index of ENSO variability) and two upper ocean quantities from Maud Rise region over past 20 years [from Martinson and Iannuzzi, submitted manuscript, 2000]: (1) solid circles with bold scatter bars (1σ) are a measure of upper ocean bulk stability (the amount of buoyancy that must be removed in order to induce deep convection, given as z scores, i.e., standard deviations from mean), and (2) crosses with dashed error bars as winter average upper ocean heat flux (again, given in z scores). The large scatter in heat flux values reflects the strong spatial variability in the Maud Rise region. The histogram shown below the time series and labeled as “Instantaneous Correlation” shows where the large correlation is being realized. This statistic is developed by Martin and Iannuzzi (submitted manuscript, 2000) and shows that most of the large correlation is due to the strong covariability between Maud Rise and ENSO-associated variabilities during the two highest extreme ENSO years. (b) EOF showing coherent spatial covariability of bulk stability throughout Weddell Gyre region. This is the third EOF from Martinson and Iannuzzi (submitted manuscript, 2000). It describes 9% of the total variance and is dominated by interannual variability through the core of the gyre, encompassing Maud Rise. The temporal variability of this mode covaries with ENSO and is dominated by changes in properties of T_{max} water (e.g., its depth and temperature).

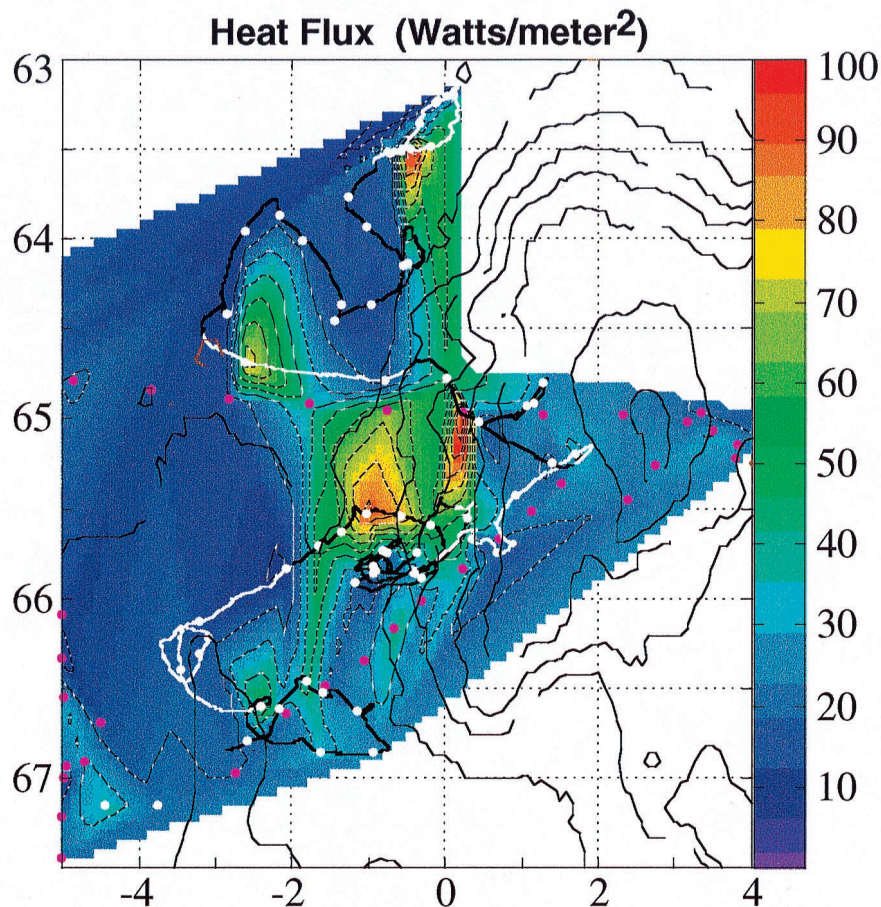


Plate 6. Upward oceanic heat flux at 10 m depth computed using *McPhee et al.*'s [1999] method applied to the grid-averaged elevation of T above freezing. A calculated area mean $u^* = 1.12 \text{ cm s}^{-1}$ was used. As for Plate 4, colored dots refer to locations of CTD casts, while white dots show locations for buoy castlets.

4.3. Local Ice Cover

Within days of the end of sampling at the second drifting site over eastern Maud Rise, satellite Special Sensor Microwave Imager (SSM/I) data revealed a large region of very low ice concentration situated a few tens of kilometers northeast of the site (M. Drinkwater, Jet Propulsion Laboratory, personal communication, 1994). We interpret this region as a polynya characterized, within limits imposed by interpretation of the SSM/I data, either by open water or by thin and wet ice cover. Such a polynya can result from large upward heat fluxes associated with ice-generated turbulence acting on the shallow thermocline over the warm pool eddies and halo west of Maud Rise and melting most of the already thin existing ice cover. The resulting polynya would then, consistent with our observations, have been advected northeast with pack ice in response to southwesterly winds, which persisted for several days after we vacated the site.

The thin ice cover and subsequent polynya formation in winter 1994 was not an unusual occurrence for the Maud Rise region. Ice concentration data presented by *Gloersen et al.* [1992] shows that by October this region typically has lower concentrations than the surrounding waters. Intermittent polynyas have been observed there in previous winters [*Comiso and Gordon*, 1987; *Gordon and Comiso*, 1988; *Gordon and Huber*, 1995]. *Comiso and Gordon* [1987] attributed the intermittent winter polynyas to introduction of warm deep water to

the surface through deep convection. *Orsi et al.* [1993] noted isolated patches of water having anomalously high T and attributed these to localized diapycnal mixing induced by bottom topography. For this to occur the thermocline must shoal locally, and we have shown that such shoaling is associated with the Maud Rise halo and with the warm pool region. Persistent high winds roughly paralleling the trend of the halo over the western flank of the rise and the hypothetically northeast-southwest oriented warm pool would be especially conducive to polynya formation. Rapidly ablating ice would continue to drift over the warm features, subjecting it to continuous melting over an extended period. Mean ice drift speeds measured during the two 6 day drifts in winter 1994 were $O(30) \text{ cm s}^{-1}$ or, roughly 30 km d^{-1} in an eastward direction, and maximum ice basal ablation rates were as high as about 10 cm d^{-1} during the periods of highest drift speed. Typical monthly mean ice drift velocities in this region are $5\text{--}10 \text{ cm s}^{-1}$ and eastward to northeastward [*Kottmeier and Sellmann*, 1996]. If the ice were to drift for a week or so within the region of elevated thermocline, then upward heat flux would be more than sufficient to melt the typically thin ($O(50) \text{ cm}$) ice cover and generate a polynya. In the extreme case, deep convecting oceanic chimneys would occur such that a large upward heat flux would prevent ice formation. This has been shown to be consistent with Taylor column formation over Maud Rise by *Alverson and Owens* [1996].

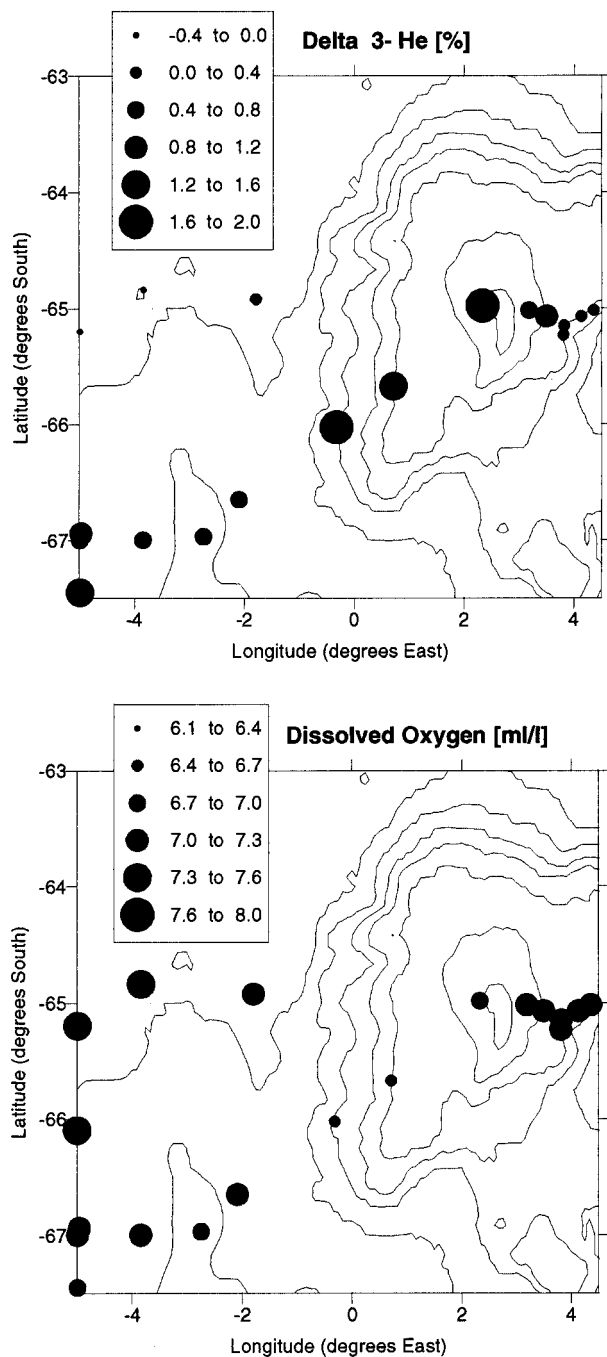


Figure 7. Average mixed layer (top) $\delta^3\text{He}$ and (bottom) DO concentrations in the Maud Rise region during the AN-ZFLUX experiment. The mixed layer depth was determined from bottle and CTD data at each station.

The occurrence of regional conditions favorable to polynya formation appears to depend also on larger-scale phenomena that vary interannually. While the mean winter heat fluxes presented above agree closely with winter climatological average heat fluxes estimated for the eastern Weddell Gyre on the basis of upper ocean properties and previously derived scaling laws [Martinson and Iannuzzi, 1998], low heat fluxes and reduced upper ocean stability typically coincide with El Niño events (Plate 5a) (Martinson and Iannuzzi, submitted manuscript, 2000). During these events the eastern Weddell Sea is

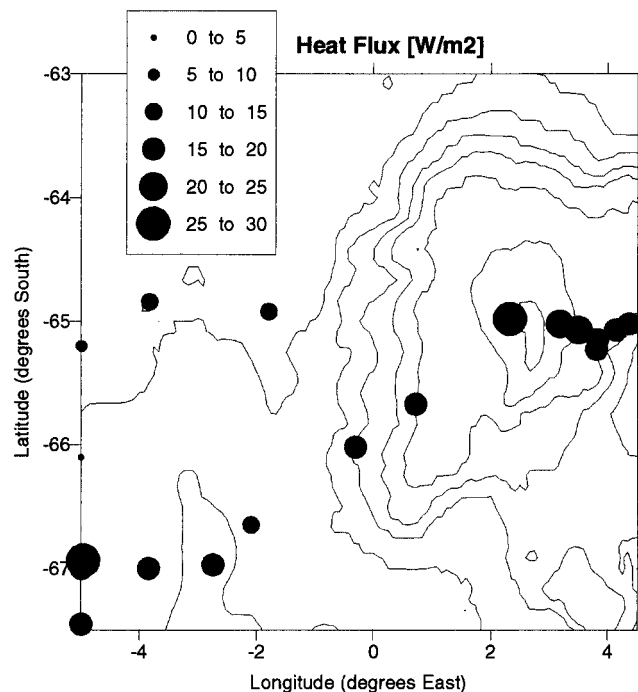


Figure 8. Winter period entrainment heat flux from the WDW into the upper mixed layer in the Maud Rise region derived from the distribution of $\delta^3\text{He}$.

most susceptible to deep convection and polynya formation because both upper ocean stability and a high heat flux act to stabilize the system with respect to salt-driven free convection driven by in situ ice growth. Hence changes in heat flux and upper ocean stability covary negatively in such a way as to increase the eastern Weddell Sea's resistance to deep convection.

5. Summary

Our results provide new and detailed documentation of oceanographic conditions in the vicinity of Maud Rise and expand upon past work that has addressed vertical upper ocean heat flux and ice cover in the region.

1. The warm pool region southwest of the rise is seen to be a dynamically necessary region of cyclonic vorticity that is associated with a Taylor column over Maud Rise. The warm pool should more precisely be described as a region of warm-core eddies and filaments that lies downstream from Maud Rise and has a mean positive vorticity through its dynamic linkage to the Taylor column overlying the rise.

2. The closed circulation, or warm halo, about Maud Rise and the warm pool are both associated with thermocline shoaling that is a necessary condition for high upward heat fluxes to occur. The influence of Maud Rise bottom topography on the upper ocean heat flux consequently extends over a region that is larger, by a factor of at least 2, than the area directly overlying the Rise.

3. Areal mean upward heat fluxes, derived using both upper ocean T (instantaneous) values and tracer-based (integrated) values, were about 25 W m^{-2} over the halo and the warm pool. Values derived over the core halo and warm pool regions using only upper ocean T exceeded 100 W m^{-2} at some sites. Elsewhere in the region, the T -derived heat fluxes varied

widely ($<10\text{--}50\text{ W m}^{-2}$), whereas the tracer-derived heat fluxes showed a much smoother distribution and typical values near 15 W m^{-2} . Our mean values are close to those that have been previously reported. Historical ice cover data has shown that the geographical region encompassed by Maud Rise and the warm pool area to the southwest is a preferred site for polynya formation, consistent with these high heat fluxes.

Acknowledgments. The research reported here has been supported by the U.S. National Science Foundation through grants OPP-9315019 to Earth & Space Research (RDM), grant support to the University of Washington (JHM), OPP-9317321 and OPP-9615524 to Oregon State University subcontracted to Earth & Space Research as OPP-9896041 (LP), and OPP-9317231 and OPP-9528807 to Lamont-Doherty Earth Observatory (DGM, PS, BH, and RH). We are indebted to Robin Tokmakian of the Naval Postgraduate School for providing us with output from, and advice concerning, the Semtner-Chervin POCM and to Christoph Kottmeier of the University of Karlsruhe, Germany, for providing us with data from the AWI drifting buoy. This work could not have been done without assistance from the captain, crew, and support staff of the RVIB *Nathaniel B. Palmer*. This is Earth & Space Research contribution 022 and LDEO contribution 6120.

References

- Alverson, K., and W. B. Owens, Topographic preconditioning of open-ocean deep convection, *J. Phys. Oceanogr.*, **26**, 2196–2213, 1996.
- Barnier, B., L. Siefried, and P. Marchesiello, Thermal forcing for a global ocean circulation model using a 3-year climatology of ECMWF, *J. Mar. Syst.*, **6**, 363–380, 1995.
- Benson, B. B., and D. Krause, Isotopic fractionation of helium during solution: A probe for the liquid state, *J. Solution Chem.*, **9**, 895–909, 1980.
- Bersch, M., G. A. Becker, H. Frey, and K. P. Koltermann, Topographic effects of the Maud Rise on the stratification and circulation of the Weddell Gyre, *Deep Sea Res., Part A*, **39**, 303–331, 1992.
- Brink, K. H., Tidal and lower frequency currents above Fieberling Guyot, *J. Geophys. Res.*, **100**, 10,817–10,832, 1995.
- Clarke, W. B., W. J. Jenkins, and Z. Top, Determination of tritium by mass spectrometric measurement of ^3He , *Int. J. Appl. Radiat. Isot.*, **27**, 515–522, 1976.
- Comiso, J. C., and A. L. Gordon, Recurring polynyas over the Cosmonaut Sea and the Maud Rise, *J. Geophys. Res.*, **92**, 2819–2833, 1987.
- De Veaux, R. D., A. L. Gordon, J. C. Comiso, and N. E. Bacherer, Modeling of topographic effects on Antarctic sea-ice using multivariate adaptive regression splines, *J. Geophys. Res.*, **98**, 20,307–20,319, 1993.
- Fahrbach, E., M. Schröder, and A. Klepikov, Circulation and water masses in the Weddell Sea, in *Physics of Ice-Covered Seas*, vol. 2, pp. 569–603, Helsinki Univ. Press, Helsinki, Finland, 1998.
- Gloersen, P., W. J. Campbell, D. J. Cavalieri, J. C. Comiso, C. L. Parkinson, and H. J. Zwally, Arctic and Antarctic sea ice, 1978–1987: Satellite passive-microwave observations and analysis, *NASA Spec. Publ.*, **511**, 290 pp., 1992.
- Goldner, D. R., and D. C. Chapman, Flow and particle motion induced above a tall seamount by steady and tidal background currents, *Deep Sea Res., Part I*, **44**, 719–744, 1997.
- Gordon, A. L., and J. C. Comiso, Polynyas and the Southern Ocean, *Science*, **258**, 90–97, 1988.
- Gordon, A. L., and B. A. Huber, Thermohaline stratification below the Southern Ocean sea ice, *J. Geophys. Res.*, **89**, 641–648, 1984.
- Gordon, A. L., and B. A. Huber, Southern Ocean winter mixed layer, *J. Geophys. Res.*, **95**, 11,655–11,672, 1990.
- Gordon, A. L., and B. A. Huber, Warm Weddell Deep Water west of Maud Rise, *J. Geophys. Res.*, **100**, 13,747–13,753, 1995.
- Gouretski, V. V., and A. I. Danilov, Weddell Gyre: Structure of the eastern boundary, *Deep Sea Res., Part I*, **40**, 561–582, 1993.
- Kaplan, A., Y. Kushnir, M. A. Cane, and M. B. Blumenthal, Reduced space optimal analysis for historical datasets: 136 years of Atlantic sea surface temperature, *J. Geophys. Res.*, **102**, 27,835–27,860, 1998.
- Kottmeier, C., and L. Sellmann, Atmospheric and oceanic forcing of Weddell Sea ice motion, *J. Geophys. Res.*, **101**, 20,809–20,824, 1996.
- Levitus, S., Climatological atlas of the world ocean, *NOAA Prof. Pap.*, **13**, 173 pp., 1982.
- Levitus, S., and T. P. Boyer, *World Ocean Atlas 1994*, vol. 4, *Temperature*, NOAA Atlas NESDIS, vol. 4, 129 pp., Natl. Oceanic and Atmos. Admin., Silver Spring, Md., 1994.
- Levitus, S., R. Burgett, and T. Boyer, *World Ocean Atlas 1994*, vol. 3, *Salinity* NOAA Atlas NESDIS, vol. 3, 111 pp., Natl. Oceanic and Atmos. Admin., Silver Spring, Md., 1994.
- Ludin, A., R. Weppernig, G. Bönisch, and P. Schlosser, Mass spectrometric measurement of helium isotopes and tritium in water samples, *LDEO Tech. Rep.*, 98-6, Lamont-Doherty Earth Observ., Palisades, N. Y., 1998.
- Martinson, D. G., Evolution of the Southern Ocean winter mixed layer and sea ice: Open ocean deep water formation and ventilation, *J. Geophys. Res.*, **95**, 11,641–11,654, 1990.
- Martinson, D. G., and R. A. Iannuzzi, Antarctic ocean-ice interaction: Implications from ocean bulk property distributions, in *Sea Ice: Physical Processes, Interactions and Variability*, *Antarct. Res. Ser.*, vol. 74, edited by M. O. Jeffries, pp. 243–271, AGU, Washington, 1998.
- McPhee, M. G., S. F. Ackley, P. Guest, B. A. Huber, D. G. Martinson, J. H. Morison, R. D. Muench, L. Padman, and T. P. Stanton, The Antarctic Flux Zone Experiment, *Bull. Am. Meteorol. Soc.*, **77**, 1221–1232, 1996.
- McPhee, M. G., C. Kottmeier, and J. H. Morison, Ocean heat flux in the central Weddell Sea during winter, *J. Phys. Oceanogr.*, **29**, 1166–1179, 1999.
- Orsi, A. H., W. D. Nowlin, Jr., and T. Whitworth III, On the circulation and stratification of the Weddell Gyre, *Deep Sea Res., Part I*, **40**, 169–203, 1993.
- Ou, H. W., Some effects of a seamount on oceanic flows, *J. Phys. Oceanogr.*, **21**, 1835–1845, 1991.
- Padman, L., A. J. Plueddemann, R. D. Muench, and R. Pinkel, Diurnal tides near the Yermak Plateau, *J. Geophys. Res.*, **97**, 12,639–12,652, 1992.
- Robertson, R., L. Padman, and G. D. Egbert, Tidal currents in the Weddell Sea, in *Ocean, Ice and Atmosphere: Interactions at the Antarctic Continental Margin*, edited by S. S. Jacobs and R. F. Weiss, *Antarct. Res. Ser.*, vol. 75, pp. 341–369, AGU, Washington, D. C., 1998.
- Schlosser, P., W. Roether, and G. Rohardt, Helium-3 balance of the upper layers in the northwestern Weddell Sea, *Deep Sea Res., Part A*, **34**, 365–377, 1987.
- Schlosser, P., R. Bayer, A. Foldvik, T. Gammelsrød, G. Rohardt, and K. O. Münnich, ^{18}O and helium isotopes as tracers of Ice Shelf Water and water/ice interaction in the Weddell Sea, *J. Geophys. Res.*, **95**, 3253–3263, 1990.
- Schweitzer, P. N., B. Babbit, and G. Eaton, Monthly average polar sea ice concentration [CD-ROM], *U.S. Geol. Surv. Digital Ser.*, DDS-27, 1995.
- Semtner, A. J., and R. M. Chervin, Ocean general circulation from a global eddy-resolving model, *J. Geophys. Res.*, **97**, 5493–5550, 1992.
- Stammer, D., R. Tokmakian, A. J. Semtner, and C. Wunsch, How well does 1/4 deg. circulation model simulate large-scale oceanic observations?, *J. Geophys. Res.*, **101**, 25,779–25,811, 1996.
- Wadhams, P., M. A. Lange, and S. F. Ackley, The ice thickness distribution across the Atlantic sector of the Antarctic Ocean in mid-winter, *J. Geophys. Res.*, **92**, 14,535–14,552, 1987.
- Wamser, C., and D. G. Martinson, Drag coefficients for winter Antarctic pack ice, *J. Geophys. Res.*, **98**, 12,431–12,437, 1993.
- Weiss, R. F., The solubility of nitrogen, oxygen and argon in water and seawater, *Deep Sea Res., Oceanogr. Abstr.*, **17**, 721–735, 1970.

R. Hohmann, B. Huber, D. Martinson, and P. Schlosser, Lamont-Doherty Earth Observatory, P.O. Box 1000, Palisades, NY 10964–8000.

J. H. Morison, Polar Science Center, APL, 1013 NE 40th Street, Seattle, WA 98105.

R. D. Muench and L. Padman, Earth & Space Research, 1910 Fairview E., Suite 102, Seattle, WA 98102–3620. (rmuench@esr.org)

(Received July 3, 2000; accepted August 31, 2000.)